Nano Research
2020, 13(12): 3241–3247
ISSN 1998-0124 CN 11-5974/O4
https://doi.org/10.1007/s12274-020-2996-1

Research Article

3D RNA nanocage for encapsulation and shielding of hydrophobic biomolecules to improve the *in vivo* biodistribution

Congcong Xu[1], Kaiming Zhang[2], Hongran Yin[1], Zhefeng Li[1], Alexey Krasnoslobodtsev[3,4], Zhen Zheng[1], Zhouxiang Ji[1], Sijin Guo[1], Shanshan Li[2], Wah Chiu[2,5], and Peixuan Guo[1] (✉)

[1] *Center for RNA Nanobiotechnology and Nanomedicine, College of Pharmacy, Division of Pharmaceutics and Pharmaceutical Chemistry, College of Medicine, Dorothy M. Davis Heart and Lung Research Institute, James Comprehensive Cancer Center, The Ohio State University, Columbus, OH 43210, USA*
[2] *Department of Bioengineering, James H. Clark Center, Stanford University, Stanford, CA 94305, USA*
[3] *Department of Physics, University of Nebraska at Omaha, Omaha, NE 68182, USA*
[4] *Nanoimaging Core Facility, Office of Vice-Chancellor for Research, University of Nebraska Medical Center, Omaha, NE 68198, USA*
[5] *SLAC National Accelerator Laboratory, Stanford University, Menlo Park, CA 94025, USA*

Received: 9 June 2020 / **Revised:** 16 July 2020 / **Accepted:** 18 July 2020

ABSTRACT

Ribonucleic acid (RNA) nanotechnology platforms have the potential of harboring therapeutics for *in vivo* delivery in disease treatment. However, the nonspecific interaction between the harbored hydrophobic drugs and cells or other components before reaching the diseased site has been an obstacle in drug delivery. Here we report an encapsulation strategy to prevent such nonspecific hydrophobic interactions *in vitro* and *in vivo* based on a self-assembled three-dimensional (3D) RNA nanocage. By placing an RNA three-way junction (3WJ) in the cavity of the nanocage, the conjugated hydrophobic molecules were specifically positioned within the nanocage, preventing their exposure to the biological environment. The assembly of the nanocages was characterized by native polyacrylamide gel electrophoresis (PAGE), atomic force microscopy (AFM), and cryogenic electron microscopy (cryo-EM) imaging. The stealth effect of the nanocage for hydrophobic molecules *in vitro* was evaluated by gel electrophoresis, flow cytometry, and confocal microscopy. The *in vivo* sheathing effect of the nanocage for hydrophobic molecules was assessed by biodistribution profiling in mice. The RNA nanocages with hydrophobic biomolecules underwent faster clearance in liver and spleen in comparison to their counterparts. Therefore, this encapsulation strategy holds promise for *in vivo* delivery of hydrophobic drugs for disease treatment.

KEYWORDS

ribonucleic acid (RNA) nanocage, three-way junction (3WJ), encapsulation, hydrophobic biomolecule, RNA nanotechnology

1 Introduction

The past decades witnessed the rapid development of nanotechnology-enabled therapeutics and medical devices [1]. However, the biggest hurdle to the clinical translation of nanotechnology lies in the biological barriers wherein the nonspecific cellular interaction and undesirable organ accumulation occur [2, 3]. Accumulation of nanoparticles in healthy organs, such as liver, spleen, and kidneys, can lead to toxicity and lower efficacy of the administered nanoparticles [4, 5]. As the *in vivo* journey of nanoparticles is critically impacted by their physicochemical properties, much effort has involved in the creation of nanoparticles with diverse size, shape, and surface characteristics to modulate the pharmacokinetic profiles.

Various nanoparticles have been investigated extensively for the treatment of disease, for example, polymers [6, 7], gold nanoparticles [8, 9], liposomes [10, 11], silica nanoparticles [12, 13], ceramics [14], iron oxides [15, 16], and deoxyribonucleic acid (DNA) nanoparticle [17–19] have shown promises. Ribonucleic acid (RNA), as a special class of polymers with unique properties, could be used as a building material to controllably self-assemble nanostructures with defined size, shape, and stoichiometry [20–22]. By virtue of its highly tunable pattern with high thermostability, RNA nanoparticles have been developed for delivery of potent anti-cancer therapeutics [23–25]. The advantage of using RNA nanoparticles for therapy is as follows [26–28]:

1) The negative charge avoids nonspecific binding to negatively charged cell membrane;

2) Controlled synthesis with defined structure and stoichiometry;

3) Multi-valency to harbor small interfering RNA (siRNA), micro RNA (miRNA), ribozyme, riboswitch, fluorophore, drugs, aptamers, ligands, and drugs;

4) Therapy targeting and detection can be combined into one particle;

5) Targeted delivery enhances local concentration and allows for specific cell entry or receptor-mediated endocytosis;

6) Advantageous size of 10–20 nm is large enough to avoid nonspecific diffusion into cells but small enough to avoid nonspecific entry to organs trapped by macrophage;

Address correspondence to guo.1091@osu.edu

7) Its fast body execration within several hours after systemic injection reduces the toxicity and side effect;

8) The nonproteins nature eliminates issues with antibody induction, allowing for repeated treatment of chronic diseases;

9) RNA nanoparticles are not biologically produced in a living system, but rather manufactured through chemical synthesis. As a result, the structure, shape, and physical/chemical properties are known; homogeneity can be achieved; and quality control is simpler;

10) The favorable size lead to favorable pharmacokinetics (PK). Fast clearance (Cl) in circulation and organ, but low in tumor (< 0.13 $kg^{-1}·h^{-1}$) with large volume distribution (V(d) ~ 1.2 kg^{-1});

11) RNA nanoparticles are classified as chemical drugs rather than biological entities. This classification facilitates drug approval.

With a growing number of RNA nanoparticles being constructed as nanocarriers, a closer look at their interactions with biological milieu will provide useful insights [29]. Recent studies on two-dimensional (2D) RNA polygons such as triangle, square, and pentagon have elucidated the effects of size and shape on their *in vivo* biodistribution profiles [30]. Different sizes and shapes of RNA nanostructures led to different circulation time and excretion pathways. Additionally, studies have shown that the hydrophobic chemicals conjugated to RNA nanoparticles induced more significant organ accumulation, thus posing a challenge in bypassing the biological barriers when the conjugated hydrophobic drug molecules are exposed to biological environment [31]. To prevent such strong hydrophobic interactions, the hydrophilic framework of RNA could be used for the protection of hydrophobic molecules from nonspecifically interacting with biological membranes and proteins. Thus, three-dimensional (3D) RNA nanocage (NC) with inner cavity for loading of hydrophobic molecules is a desirable approach. As shown in Scheme 1, RNA NCs of different surface characteristics will presumably exhibit different nano–bio interface behavior at the cellular membrane level as well as serum protein binding level. When the hydrophobic molecules are present on the surface of NC (i.e., displaying mode), it would lead to stronger membrane interaction and serum protein binding as more hydrophobic surface of nanoparticle is more likely to nonspecifically bind to lipid membrane and absorb serum proteins [32, 33]. In contrast, when the hydrophobic molecules are loaded in the cavity of nanocage (i.e., encapsulation mode), undesirable interactions with cell membranes and serum proteins could be reduced.

Here we report a simple design of a 3D RNA NC with inner cavity for precise encapsulation of hydrophobic biomolecules based on naturally occurring RNA motifs. We specifically encapsulated the 5S three-way junction (3WJ) carrying cholesterol as model hydrophobic drug molecules into the pyramid-shaped RNA NC. The successful assembly of the NC with displayed or encapsulated cargo was characterized by native polyacrylamide gel electrophoresis (PAGE), atomic force microscopy (AFM), as well as cryogenic electron microscopy (cryo-EM). *In vitro* flow cytometry analysis and confocal microscopy imaging demonstrated the reduced nonspecific interaction of NC with cells and cell-mimicking vesicles, respectively. *In vivo* biodistribution profiling results exhibited the significantly reduced retention of RNA NC in liver and spleen when the hydrophobic cholesterol was encapsulated compared to its displaying counterpart. Hence, the encapsulation strategy using RNA NC provides a promising solution to address the concerns of *in vivo* hydrophobic drug delivery.

2 Results and discussion

2.1 Computer-aided design and construction of 3D RNA NC for cargo display and encapsulation

The modular design of the RNA nanocage was primarily based on several naturally occurring RNA motifs following a bottom-up assembly approach. The 3WJ motif (PDB entry: 4KZ2, Fig. 1(a)) of packaging RNA (pRNA) [23] and the four-way junction (4WJ) motif of a hairpin ribozyme molecule were hinged on by the RNA duplex to form an intact pyramid-shaped nanocage (Fig. 1(b))[34]. 3WJ module was placed at each corner of the RNA NC and the 4WJ motif was placed at the vertex linking to all 3WJ modules. To display cargos on the surface of NC, two of the strands (P2E, P4E) were extended with dangling ends at the nick position to produce diagonal protruding sticky ends, thus enabling the hybridization of complementary sequences with cargo (top view with sequence, Fig. S1(a) in the Electronic Supplementary Material (ESM)). To design a similar NC for encapsulation, a new 5S 3WJ motif was positioned within the NC by incorporation of the 5S 3WJb sequence into P24 strand (top view with sequence, Fig. S1(b) in the ESM) (Fig. 1(c))[35], which forms a connecting bridge within the cavity of NC. Upon assembly with 5S a and 5S c strands, a 5S 3WJ forms within NC. All synthesized RNA oligos (Fig. S2 in the ESM, see the detailed sequence in Tables S1 and S2 in the ESM) were *in vitro* one-pot self-assembled into a pyramid-shaped NC (Fig. S3 in the ESM) with 4 triangular side faces and 1 square bottom face composed of 8 double-stranded edges. The extended NC (NC-Ext) displays 2 dangling ends on the surface while the NC with internalized 3WJ (NC-Int) encapsulates 5S 3WJ motif conjugated with cargo. Swiss PDB viewer (http://www.expasy.org/spdbv/) and PyMOL Molecular Graphics System (https://www.pymol.org/) were used to align 4 corners and vertices with RNA helix linkage. One-pot self-assembly of the NCs was achieved by thermal denaturation of equimolar RNA oligonucleotides at 85 °C,

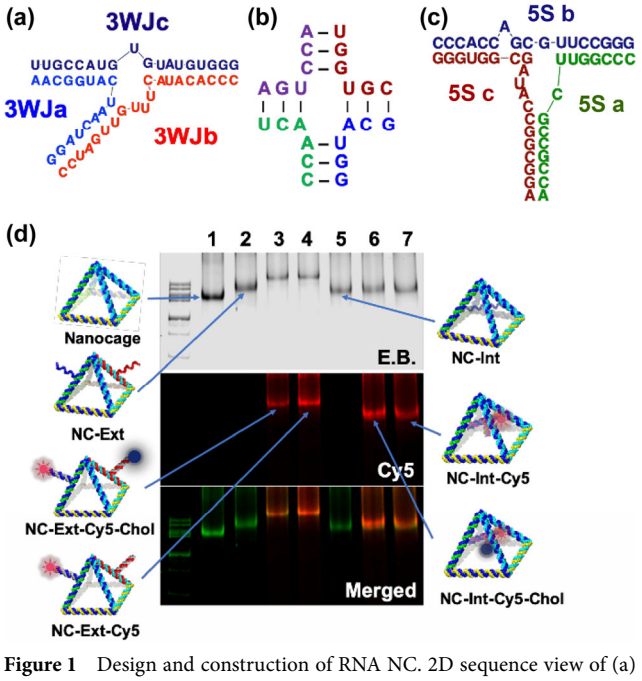

Figure 1 Design and construction of RNA NC. 2D sequence view of (a) phi29 3WJ, (b) 4WJ core derived from a hairpin ribozyme and (c) 5S 3WJ. (d) Native PAGE characterization of NCs with displayed and encapsulated biomolecules.

followed by an annealing process (slowly cooling down to 4 °C over 45 min). To obtain intact RNA NC nanoparticles, component strands were mixed in stoichiometric ratio to form complex with high efficiency.

To verify the stepwise assembly of RNA NC-Ext and NC-Int, a native 6% PAGE experiment was carried out (Figs. S4(a) and S4(b) in the ESM). Component strands were gradually added into the mixture for assembly followed by gel analysis to verify the participation of each strand in the assembled complex. To load bioactive compounds on NC-Ext and NC-Int nanoparticles, cholesterol modified P4E and 5S c strands were co-assembled respectively with NC framework strands. As a highly lipophilic biomolecule, cholesterol has strong interactions with phospholipid membrane. Therefore, we used cholesterol as a model drug for encapsulation, thereby preventing its interaction with cell membranes at the nano–bio interface. As shown in 6% native PAGE gel, electrophoretic mobility in lanes 1–6 (Fig. S4(a) in the ESM) and in lanes 1–4 (Fig. S4(b) in the ESM) indicated a stepwise upshift due to the increased strand composition in the complex. For NC-Ext assembly, upon hybridization with two other short strands (P2E-comp-Cy5, P4E-comp-Chol), a slight upshift in gel mobility was observed (lanes 2–4 in Fig. 1(d)) while NC-Int did not show noticeable gel mobility shift after incorporation of 2 other strands (5S a-Cy5, 5S c-Chol) (lanes 5–7 in Fig. 1(d)) probably due to the less effects on electrophoretic mobility while strands are encapsulated within the cavity of complex. Cy5 fluorophore labeled strands further suggested the incorporation of short strand within the RNA NC as imaged in Cy5 channel (Fig. 1(d)).

2.2 Physicochemical characterization of RNA NCs

As the physicochemical properties of nanoparticles such as size, shape, and thermostability are closely related to their *in vivo* behavior [4], we first characterized the 2 different NCs in terms of their size and thermostability. The average hydrodynamic diameter of NCs was measured using dynamic light scattering (DLS) assay. As revealed in Fig. S5(a) in the ESM, the apparent hydrodynamic size of NC-Ext and NC-Int turned out to be 14.1 ± 3.0 and 13.8 ± 3.1 nm, respectively. Despite of the pyramidal shape of RNA NCs, we assumed that the reported size was in good agreement with the predicted size, considering the rapid tumbling of RNA nanoparticles in solution. Two NCs exhibit similar hydrodynamic size probably due to the fact that the dangling ends on NC-Ext are flexible. We also investigated the size after incorporation of cholesterol and Cy5 fluorophore on NCs. No significant changes in hydrodynamic size were observed as shown in Fig. S5(b) in the ESM. To compare the stability of assembled NCs, the thermo-stability of NC-Ext and NC-Int was investigated by temperature gradient gel electrophoresis (TGGE). TGGE is commonly used for measuring melting temperature (T_m) of large and complex nucleic acids structures [36]. A gradient temperature (40–80 °C) was applied perpendicular to the electrical current on the 4% native polyacrylamide gel, with an increasing temperature that gradually leads to the dissociation of RNA nanostructures (Fig. S6 in the ESM). As suggested in Fig. S5(c) in the ESM, half of the NC-Ext and NC-Int remained intact at 63 and 69 °C (T_m), respectively, suggesting the high thermodynamic stability of both nanocage nanostructures. Taken together, the results from PAGE, TGGE, and DLS demonstrated the self-assembly of programmable, thermodynamically stable and intact RNA NCs.

2.3 Morphological characterization of RNA NC by cryo-EM and AFM imaging

To explore the structural characterization of 3D RNA NCs in their native states, the single particle cryo-EM analysis and 3D reconstruction were performed (Fig. 2). Around 2,100 and 1,300 selected particles for NC-Ext and NC-Int, respectively, were used for final 3D refinement, with 24-Å and 26-Å resolution maps achieved (Figs. 2(a) and 2(b)). The cryo-EM images for both NCs clearly revealed individual particles (Figs. 2(c) and 2(d)). As expected, the 3D reconstructions of NC-Ext and NC-Int showed the pyramidal shape with the extra density outside and inside, respectively. The arrows indicate the protruding density outside of NC for NC-Ext. 2D projections computed from the 3D reconstructions showed a clear match to the 2D class averages of the raw particles (Figs. 2(e) and 2(f)), suggesting that the reconstructed 3D models truly represent the native structures of the designed RNA NCs.

To visualize and validate the pyramid-shaped structure of both NCs, we performed AFM imaging and cryo-EM single-particle analysis. The NC-Ext and NC-Int were well distributed, as shown in the AFM images (Figs. 2(g) and 2(h)). Since the nanoparticle samples were deposited on 1-(3-aminopropyl)-silatrane (APS)-modified mica surface, the 3D NCs were flattened. Majority of the observed shapes appeared triangular

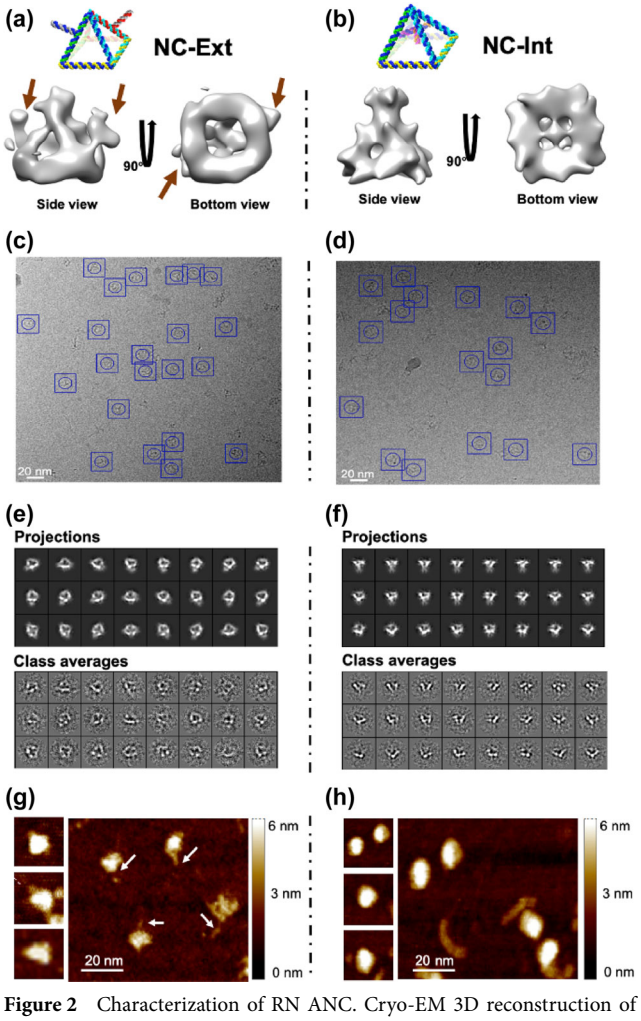

Figure 2 Characterization of RN ANC. Cryo-EM 3D reconstruction of (a) NC-Ext and (b) NC-Int. Single particle raw images of (c) NC-Ext and (d) NC-Int. Computed 2D projections from 3D reconstructions and their related 2D class averages (e) NC-Ext and (f) NC-Int. AFM imaging of (g) NC-Ext and (h) NC-Int. Arrows indicate the dangling ends on the surface of NC-Ext.

in the AFM topography images corresponding to the side views of collapsed pyramidal NCs. The arrows indicate the protruding dangling ends of NC for NC-Ext (Fig. 2(g)). More amplified AFM images supported the side-views of pyramidal shape as well (Fig. S7 in the ESM). Due to the resolution limit of AFM probe, the detailed cavity structure of NC-Int as well as the flanking ends of NC-Ext could not be clearly resolved. Taken together with the cryo-EM characterization, the results confirmed the formation of the RNA NCs nanoparticles with good quality.

2.4 The stealth effect of the NC for hydrophobic molecules investigated by flow cytometry

To compare the interaction of different NCs with cells, we performed flow cytometry analysis using 3 cancer cell lines (KB, HT-29. and MCF-7). Given the negatively charged backbone of RNA molecules, RNA nanoparticles with hydrophobic molecules inside may avoid the nonspecific interaction with cell membranes. When the cholesterol was present on the surface of NC, it induced strong interactions with cell membranes (Fig. 3(a)) [37]. Among all the tested groups, the NC-Ext-Cy5-Chol exhibited the strongest cellular interactions in all the 3 cell lines. In contrast, when the cholesterol was loaded within the NC, it displayed similar cell interactions as NC-Int-Cy5 and NC-Ext-Cy5, demonstrating the stealth effect of hydrophilic RNA NC framework. The mean fluorescence intensity (MFI) of each analysis was plotted in Fig. 3(b). The KB cells exhibited higher nonspecific interactions with all NCs though the NC-Ext-Cy5-Chol displayed the most significant fluorescent shift after incubation. Similar results were found in the plot of median fluorescence intensity from flow cytometry analysis (Fig. S8 in the ESM). In HT-29 and MCF-7 group, NC-Int-Cy5, NC-Int-Cy5-Chol, and NC-Ext-Cy5 showed little cell binding revealed by the slight fluorescent shift compared to cell only control, while NC-Ext-Cy5-Chol had much stronger cell binding indicated by the 50-fold increase in fluorescent intensity.

2.5 The shielding effect of the NC for hydrophobic molecules evaluated by confocal microscopy

Though the flow cytometry experiments well demonstrated the difference in cellular interactions in a statistically significant manner with analysis of 10,000 events per run, the active uptake of cholesterol molecules by cells may contribute to the fluorescent shift observed [38]. To rule out the active uptake by cells and further compare the interaction of different NCs with lipid membrane, giant plasma membrane vesicles (GPMVs) [39] derived from KB cells were used as cell-mimicking vesicles to investigate the nano–bio interface interaction [40]. The GPMVs were fluorescently labeled with CellMask™ Orange (similar spectrum as Cy3 fluorophore) and all NCs were labeled with Cy5 fluorophore. Confocal microscopy images were taken under Cy3 and Cy5 channel. As revealed in merged channel (Fig. 4(a)), the NC-Ext-Cy5-Chol showed strong binding to the membrane of GPMVs as revealed in the colocalized image of two channels. As illustrated in the right panel of Fig. 4(a), spherical Cy5 signal can be observed and colocalized with CellMask™ Orange signal when NC had a strong binding to the membrane (Fig. S9 in the ESM). In other cases, the electrostatic repulsion of negatively charged membrane to NCs prevented the nonspecific hydrophobic interactions (Figs. S10–S12 in the ESM). By plotting the fluorescent intensity in a straight line across the GPMVs under Cy3 and Cy5 channel (Figs. S13 and S14 in the ESM), 2 peaks of fluorescent intensity under Cy5 and Cy3 signal which referred to the signal from each side of membrane were colocalized in NC-Ext-Cy5-Chol group while other groups showed very low Cy5 colocalization with Cy3 signal (Fig. 4(b)), indicating the very low binding of NCs to GPMVs (Figs. S13 and S14 in the ESM). Following the GPMVs interaction imaging, lipid vesicles were used as another model to compare the hydrophobic interaction of cholesterol displaying and encapsulated NCs with membranes. In brief, small unilamellar vesicles (SUVs)[41] with the fluorescent label (TopFluor® TMR, similar spectrum as Cy3 fluorophore) were incubated with NCs overnight before confocal microscopy imaging. As a result of the small size of SUVs (50–100 nm), the spherical shape was not clearly seen. However, we examined the colocalization of NCs with SUVs. Similar results were found where NC-Ext-Cy5-Chol group displayed the strongest

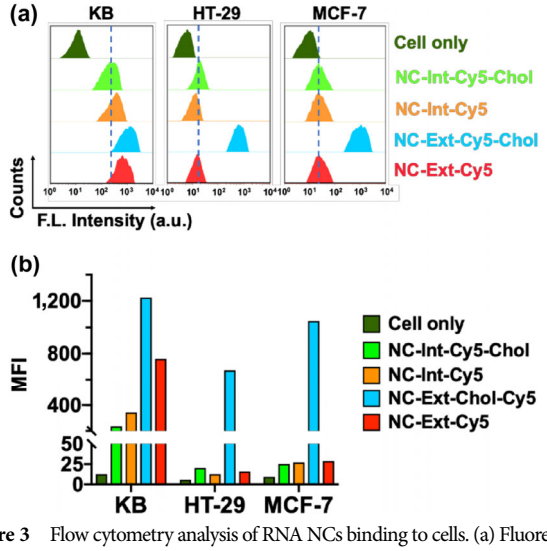

Figure 3 Flow cytometry analysis of RNA NCs binding to cells. (a) Fluorescent intensity shift profiles of cells in three cell lines. (b) MFI plot showing the fluorescent intensity shift.

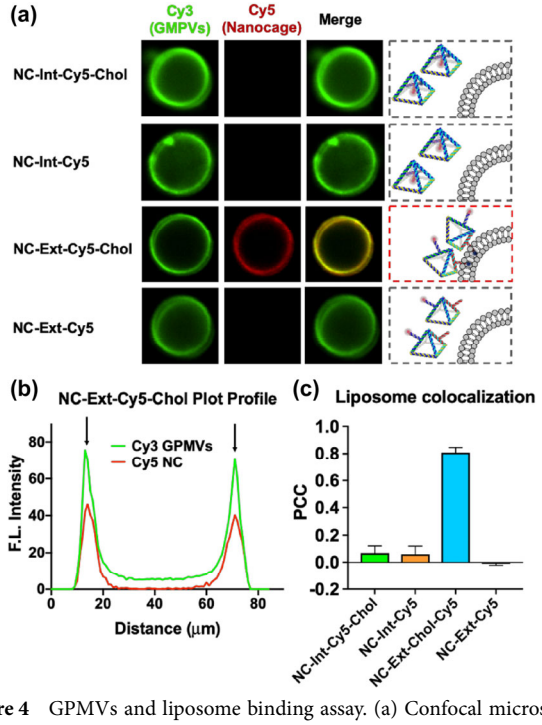

Figure 4 GPMVs and liposome binding assay. (a) Confocal microscopy imaging of pyramid NCs binding to GPMVs. (b) Plot profile of NC-Ext-Cy5-Chol showing the fluorescent intensity across the GPMVs in Cy5 and Cy3 channels. (c) PCC of different RNA NCs with SUVs. Error bars indicate the standard deviation (SD) in 5 independent measures.

binding to SUVs (Fig. S15 in the ESM). Other groups of NCs did not show noticeable binding to liposomes (Figs. S16–S18 in the ESM). Pearson's colocalization coefficient (PCC) of different NCs with liposomes was calculated in ImageJ software and plotted as Fig. 4(c). As a well-established measure of correlation, PCC has a range of +1 (perfect correlation) to −1 (perfect negative correlation) [42, 43]. When PCC is close to 0, it denotes the absence of a relationship. With a mean PCC of 0.82 found in NC-Ext-Cy5-Chol group and close to 0 in other NC groups, we assumed that the encapsulation strategy implemented on RNA NC for cholesterol could minimize the nonspecific hydrophobic interactions at the membrane interface.

2.6 Evaluation of the serum protein binding and serum stability of NCs

The *in vitro* assays at the cellular and membrane levels demonstrated the suitability of using NC to encapsulate hydrophobic cholesterol for minimal nonspecific cellular interactions. However, the biological barriers include a complex series of obstacles such as opsonization, subsequent sequestration by mononuclear phagocyte system (MPS) in liver and spleen, and nonspecific distribution [3, 44]. As the process of sequestration *in vivo* begins with opsonization of administered nanoparticles, the protein corona formation and protein adsorption on the surface of nanoparticles critically affect their biological identity [45, 46]. With a more hydrophobic surface, protein absorption becomes more significant, leading to the recognition by Kupffer cells in liver sinusoids and resident macrophages in spleen [47–50]. Therefore, we first did an *in vitro* serum protein binding comparison simply by incubating NCs with a gradient concentration of fetal bovine serum (FBS) to elucidate the effects of surface characteristics on serum protein adsorption. It was reported that the protein corona forms rapidly on nanoparticles within 0.5 min [51]. Here we incubated different NCs with a range of 0%–35% FBS in phosphate buffered saline (PBS) buffer for 5 min before 6% native PAGE characterization (Figs. S19–S21 in the ESM). By quantification of unbound NCs, we obtained the serum protein binding profiles of NC-Ext-Cy5-Chol and NC-Int-Cy5-Chol as illustrated in Fig. 5(a). With an increasing FBS, the unbound fraction for both NCs decreased dramatically. By determining the equilibrium serum concentration (i.e., the percentage of serum at which 50% of the particle is unbound), NC-Ext-Cy5-Chol reached as low as 12.1% FBS while NC-Int-Cy5-Chol achieved 50% serum binding at 18.8% FBS concentration (Fig. 5(a)). We did not observe a dramatic difference in serum binding of these 2 NCs probably due to the open cavity (9 nm × 9 nm) at the bottom of pyramidal NC which still allows the possible interaction of bovine serum albumin (BSA, 4 nm × 4 nm × 14 nm in dimension), a major component protein in FBS, with encapsulated cholesterol (see schematic dimensions in Fig S22 in the ESM). However, the subtle difference in serum protein interactions may contribute to a different *in vivo* behavior of nanoparticles. Human serum albumin (HSA) has a similar dimension as BSA; thus, we assumed the NC-Int will show similar effects in reducing human serum protein adsorption. As little is known about the protein corona formation on RNA nanoparticles, further comprehensive studies on corona composition and formation kinetics are needed.

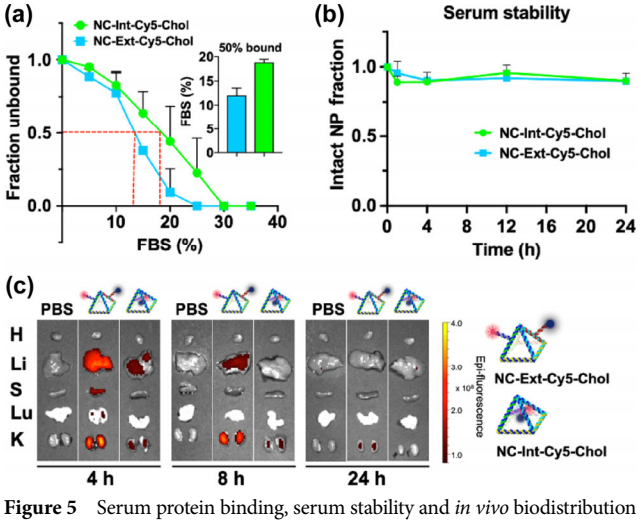

Figure 5 Serum protein binding, serum stability and *in vivo* biodistribution of RNA NCs. (a) Serum protein binding profile of NC-Ext-Cy5-Chol and NC-Int-Cy5-Chol. Small diagram shows the FBS concentration at which 50% of NCs were unbound. (b) Serum stability of NC-Ext-Cy5-Chol and NC-Int-Cy5-Chol. (c) *Ex vivo* organ images at 4, 8 and 24 h post- injection. H, heart; Li, liver; S, spleen; Lu, lung; K, kidney.

Then we compared the enzymatic stability of these two NCs. NCs labeled with Cy5 were incubated in 10% FBS solution at 37 °C. At different time points, samples were taken out and immediately frozen on dry ice to prevent further enzymatic degradation. 6% native PAGE analysis of the NCs (Figs. S23 and S24 in the ESM) revealed the comparable chemical stability of 2'-F modified NC-Ext-Cy5-Chol and NC-Int-Cy5-Chol as both two nanoparticles did not show significant degradation with up to 24 h incubation in 10% FBS buffer (Fig. 5(b)). Thus, we assumed the 2 different NCs would have similar *in vivo* serum stability.

2.7 The stealth effect of the NC for hydrophobic molecules assessed by *in vivo* biodistribution

To investigate the stealth effect of NC *in vivo*, 100 μL of 5 μM of NC-Ext-Cy5-Chol and NC-Int-Cy5-Chol were intravenously administered in BALB/c mice respectively. At post-injection 4, 8, and 24 h, the mice were sacrificed and organs (heart, liver, spleen, lung, and kidney) were collected for fluorescent imaging. Interestingly, 2 tested groups showed distinct biodistribution profiles (Fig. 5(c)). The NC-Ext-Cy5-Chol exhibited significant retention in vital organs such as liver and spleen until 8 h post-injection while its counterpart showed much less liver and spleen accumulation at 4 h post-injection. At 8 h time point, most of the NC-Int-Cy5-Chol was eliminated from liver. As a result of the protection by hydrophilic framework of NC, NC-Int-Cy5-Chol was cleared from mice quickly with less liver and spleen retention. In addition, renal clearance of NC-Ext-Cy5-Chol was still seen at 24 h post-injection, while little was seen for NC-Int-Cy5-Chol. Since glomerular filtration of nanosized macromolecules is strongly size-dependent (hydrodynamic diameter < 6 nm) [52, 53], the kidney filtration may not be applicable for RNA NCs with diameter larger than 10 nm [26]. Nevertheless, we expected that the RNA NCs might be able to pass through the endothelial layer of glomerulus and consequently blocked by the glomerular basement membrane [52]. Thus, we observed RNA NCs retention in the kidney as well. However, whether the longer retention time in kidney compartments for NC-Ext-Cy5-Chol was caused by stronger hydrophobic surface needs to be investigated. Based on the *in vitro* cellular membrane interaction as well as serum protein binding results, we suspected that the NC-Ext-Cy5-Chol displayed a stronger opsonization upon introduction into the biological environment which triggered more significant sequestration by MPS. Therefore, we observed longer retention and stronger accumulation in the liver and spleen [54]. As such, we demonstrated the shielding effect of NC for hydrophobic biomolecule *in vivo*, which could potentially be exploited to

improve the bioavailability of poorly water-soluble chemical drugs such as Paclitaxel, Camptothecin, and Oridonin. Additionally, a more quantitative biodistribution profiling strategy such as radiolabeling may be applied in the future for precise quantification of organ distribution.

3 Conclusions

Using RNA motifs as building blocks for the assembly of programmable nanoparticles holds great promises for effective *in vivo* drug delivery. Physicochemical properties of RNA nanoparticles such as size, shape, and surface chemistry have shown to impact their *in vivo* behavior [32, 55]. Here we report the controllable surface characteristics of three-dimensional NCs by loading or displaying hydrophobic model drugs within the inner cavity or on the surface, respectively. Native PAGE characterization suggested the assembly of NC-Ext and NC-Int. Further AFM and cryo-EM imaging confirmed the intact nanoparticles with a uniform pyramidal shape. The stealth effect by NC at cellular level was elucidated by *in vitro* flow cytometry analysis and confocal imaging based on cell binding, GPMVs interaction as well as SUVs colocalization. Serum protein binding assay revealed the subtle difference between NC-Int and NC-Ext in protein adsorption. Finally, we obtained a distinct *in vivo* biodistribution profiles with different surface hydrophobicity of RNA NCs. Of note, the liver and spleen retention of NC-Ext-Cy5-Chol was significantly higher than that of NC-Int-Cy5-Chol. Combining with cellular and organ level results, we could draw a conclusion that the RNA NC can be potentially used for hydrophobic drug encapsulation to achieve favorable *in vivo* biodistribution. On the other hand, a comprehensive investigation of the protein corona composition as a correlation to surface chemistry of RNA nanoparticles needs to be done in the future and more quantitative pharmacokinetics studies of RNA NCs *in vivo* will provide reliable results to understand the effects of physicochemical properties of RNA NCs.

Acknowledgements

The research in P. G.'s lab was supported by NIH grants (Nos. R01EB019036, U01CA151648, and U01CA207946) to Peixuan Guo. The cryo-EM work was supported by NIH grant No. 5941GM103832 (W. C.) and Office of Naval Research grant No. N00014-20-1-2084 (W. C.). P. G.'s Sylvan G. Frank Endowed Chair position in Pharmaceutics and Drug Delivery is funded by the CM Chen Foundation. The authors would like to thank the Nanoimaging Core Facility at UNMC for assistance with AFM imaging. The facility is in part supported by funds received from the Nebraska Research Initiative (NRI). The animal study protocol was approved by the Institutional Animal Care and Use Committee at The Ohio State University. The authors would like to thank Alyssa Castillo for help in sample preparation.

Conflict of interests

P. G. is the cofounder of ExonanoRNA LLC. He is also the consultant of Oxford Nanopore Technologies and Nanobio Delivery Pharmaceutical Co. Ltd, as well as the cofounder of Shenzhen P&Z Bio-medical Co. Ltd and its subsidiary US P&Z Biological Technology LLC. His inventions at the University of Kentucky have been licensed to Matt Holding and Nanobio Delivery Pharmaceutical Co., Ltd. The content is solely the responsibility of the authors and does not necessarily represent the official views of the NIH.

Electronic Supplementary Material: Supplementary material (methods and materials, nanoparticle characterization, confocal microscopy imaging results, etc) is available in the online version of this article at https://doi.org/10.1007/s12274-020-2996-1.

References

[1] Shi, J. J.; Kantoff, P. W.; Wooster, R.; Farokhzad, O. C. Cancer nanomedicine: Progress, challenges and opportunities. *Nat. Rev. Cancer* **2017**, *17*, 20–37.

[2] Blanco, E.; Shen, H. F.; Ferrari, M. Principles of nanoparticle design for overcoming biological barriers to drug delivery. *Nat. Biotechnol.* **2015**, *33*, 941–951.

[3] Kim, S. M.; Faix, P. H.; Schnitzer, J. E. Overcoming key biological barriers to cancer drug delivery and efficacy. *J. Control. Release* **2017**, *267*, 15–30.

[4] Zhao, Z. M.; Ukidve, A.; Krishnan, V.; Mitragotri, S. Effect of physicochemical and surface properties on *in vivo* fate of drug nanocarriers. *Adv. Drug Deliv. Rev.* **2019**, *143*, 3–21.

[5] Nel, A. E.; Mädler, L.; Velegol, D.; Xia, T.; Hoek, E. M. V.; Somasundaran, P.; Klaessig, F.; Castranova, V.; Thompson, M. Understanding biophysicochemical interactions at the nano-bio interface. *Nat. Mater.* **2009**, *8*, 543–557.

[6] Merino, S.; Martin, C.; Kostarelos, K.; Prato, M.; Vázquez, E. Nanocomposite hydrogels: 3D polymer-nanoparticle synergies for on-demand drug delivery. *ACS Nano* **2015**, *9*, 4686–4697.

[7] Yoo, W.; Yoo, D.; Hong, E.; Jung, E.; Go, Y.; Singh, S. V. B.; Khang, G.; Lee, D. Acid-activatable oxidative stress-inducing polysaccharide nanoparticles for anticancer therapy. *J. Control. Release* **2018**, *269*, 235–244.

[8] Huo, S. D.; Gong, N. Q.; Jiang, Y.; Chen, F.; Guo, H. B.; Gan, Y. L.; Wang, Z. S.; Herrmann, A.; Liang, X. J. Gold-DNA nanosunflowers for efficient gene silencing with controllable transformation. *Sci. Adv.* **2019**, *5*, eaaw6264.

[9] Cheng, X. J.; Sun, R.; Yin, L.; Chai, Z. F.; Shi, H. B.; Gao, M. Y. Light-triggered assembly of gold nanoparticles for photothermal therapy and photoacoustic imaging of tumors *in vivo*. *Adv. Mater.* **2017**, *29*, 1604894.

[10] Liu, Z.; Xiong, M.; Gong, J. B.; Zhang, Y.; Bai, N.; Luo, Y. P.; Li, L. Y.; Wei, Y. Q.; Liu, Y. H.; Tan, X. Y. et al. Legumain protease-activated TAT-liposome cargo for targeting tumours and their microenvironment. *Nat. Commun.* **2014**, *5*, 4280.

[11] Lu, J. Q.; Liu, X. S.; Liao, Y. P.; Wang, X.; Ahmed, A.; Jiang, W.; Ji, Y.; Meng, H.; Nel, A. E. Breast cancer chemo-immunotherapy through liposomal delivery of an immunogenic cell death stimulus plus interference in the IDO-1 pathway. *ACS Nano* **2018**, *12*, 11041–11061.

[12] Dogra, P.; Adolphi, N. L.; Wang, Z. H.; Lin, Y. S.; Butler, K. S.; Durfee, P. N.; Croissant, J. G.; Noureddine, A.; Coker, E. N.; Bearer, E. L. et al. Establishing the effects of mesoporous silica nanoparticle properties on *in vivo* disposition using imaging-based pharmacokinetics. *Nat. Commun.* **2018**, *9*, 4551.

[13] Durfee, P. N.; Lin, Y. S.; Dunphy, D. R.; Muñiz, A. J.; Butler, K. S.; Humphrey, K. R.; Lokke, A. J.; Agola, J. O.; Chou, S. S.; Chen, I. M. et al. Mesoporous silica nanoparticle-supported lipid bilayers (protocells) for active targeting and delivery to individual leukemia cells. *ACS Nano* **2016**, *10*, 8325–8345.

[14] Singh, D.; Dubey, P.; Pradhan, M.; Singh, M. R. Ceramic nanocarriers: Versatile nanosystem for protein and peptide delivery. *Expert Opin. Drug Deliv.* **2013**, *10*, 241–259.

[15] Hauser, A. K.; Mitov, M. I.; Daley, E. F.; McGarry, R. C.; Anderson, K. W.; Hilt, J. Z. Targeted iron oxide nanoparticles for the enhancement of radiation therapy. *Biomaterials* **2016**, *105*, 127–135.

[16] Laurent, S.; Saei, A. A.; Behzadi, S.; Panahifar, A.; Mahmoudi, M. Superparamagnetic iron oxide nanoparticles for delivery of therapeutic agents: Opportunities and challenges. *Expert Opin. Drug Deliv.* **2014**, *11*, 1449–1470.

[17] Li, S. P.; Jiang, Q.; Liu, S. L.; Zhang, Y. L.; Tian, Y. H.; Song, C.; Wang, J.; Zou, Y. G.; Anderson, G. J.; Han, J. Y. et al. A DNA nanorobot functions as a cancer therapeutic in response to a molecular

trigger *in vivo*. *Nat. Biotechnol.* **2018**, *36*, 258–264.
[18] Sun, W. J.; Ji, W. Y.; Hall, J. M.; Hu, Q. Y.; Wang, C.; Beisel, C. L.; Gu, Z. Self-assembled DNA nanoclews for the efficient delivery of crispr-cas9 for genome editing. *Angew. Chem., Int. Ed.* **2015**, *54*, 12029–12033.
[19] Zhu, G. Z.; Zheng, J.; Song, E. Q.; Donovan, M.; Zhang, K. J.; Liu, C.; Tan, W. H. Self-assembled, aptamer-tethered DNA nanotrains for targeted transport of molecular drugs in cancer theranostics. *Proc. Natl. Acad. Sci. USA* **2013**, *110*, 7998–8003.
[20] Li, H.; Lee, T.; Dziubla, T.; Pi, F. M.; Guo, S. J.; Xu, J.; Li, C.; Haque, F.; Liang, X. J.; Guo, P. X. RNA as a stable polymer to build controllable and defined nanostructures for material and biomedical applications. *Nano Today* **2015**, *10*, 631–655.
[21] Afonin, K. A.; Kasprzak, W. K.; Bindewald, E.; Kireeva, M.; Viard, M.; Kashlev, M.; Shapiro, B. A. *In silico* design and enzymatic synthesis of functional RNA nanoparticles. *Acc. Chem. Res.* **2014**, *47*, 1731–1741.
[22] Monferrer, A.; Zhang, D.; Lushnikov, A. J.; Hermann, T. Versatile kit of robust nanoshapes self-assembling from RNA and DNA modules. *Nat. Commun.* **2019**, *10*, 608.
[23] Shu, D.; Shu, Y.; Haque, F.; Abdelmawla, S.; Guo, P. X. Thermodynamically stable RNA three-way junction for constructing multifunctional nanoparticles for delivery of therapeutics. *Nat. Nanotechnol.* **2011**, *6*, 658–667.
[24] Shu, D.; Li, H.; Shu, Y.; Xiong, G. F.; Carson III, W. E.; Haque, F.; Xu, R.; Guo, P. X. Systemic delivery of anti-miRNA for suppression of triple negative breast cancer utilizing RNA nanotechnology. *ACS Nano* **2015**, *9*, 9731–9740.
[25] Yin, H. R.; Xiong, G. F.; Guo, S. J.; Xu, C.; Xu, R. C.; Guo, P. X.; Shu, D. Delivery of anti-miRNA for triple-negative breast cancer therapy using RNA nanoparticles targeting stem cell marker CD133. *Mol. Ther.* **2019**, *27*, 1252–1261.
[26] Xu, C. C.; Haque, F.; Jasinski, D. L.; Binzel, D. W.; Shu, D.; Guo, P. X. Favorable biodistribution, specific targeting and conditional endosomal escape of RNA nanoparticles in cancer therapy. *Cancer Lett.* **2018**, *414*, 57–70.
[27] Guo, S. J.; Xu, C. C.; Yin, H. R.; Hill, J.; Pi, F. M.; Guo, P. X. Tuning the size, shape and structure of RNA nanoparticles for favorable cancer targeting and immunostimulation. *WIREs Nanomedicine Nanobiotechnol.* **2020**, *12*, e1582.
[28] Jasinski, D.; Haque, F.; Binzel, D. W.; Guo, P. X. Advancement of the emerging field of RNA nanotechnology. *ACS Nano* **2017**, *11*, 1142–1164.
[29] Chiu, Y. T. E.; Li, H. Z.; Choi, C. H. J. Progress toward understanding the interactions between DNA nanostructures and the cell. *Small* **2019**, *15*, 1805416.
[30] Jasinski, D. L.; Li, H.; Guo, P. X. The effect of size and shape of RNA nanoparticles on biodistribution. *Mol. Ther.* **2018**, *26*, 784–792.
[31] Jasinski, D. L.; Yin, H. R.; Li, Z. F.; Guo, P. X. Hydrophobic effect from conjugated chemicals or drugs on *in vivo* biodistribution of rna nanoparticles. *Hum. Gene Ther.* **2018**, *29*, 77–86.
[32] Albanese, A.; Tang, P. S.; Chan, W. C. W. The effect of nanoparticle size, shape, and surface chemistry on biological systems. *Annu. Rev. Biomed. Eng.* **2012**, *14*, 1–16.
[33] Anderson, C. R.; Gnopo, Y. D. M.; Gambinossi, F.; Mylon, S. E.; Ferri, J. K. Modulation of cell responses to Ag-(MeO_2MA-*co*-OEGMA): Effects of nanoparticle surface hydrophobicity and serum proteins on cellular uptake and toxicity. *J. Biomed. Mater. Res. A* **2018**, *106*, 1061–1071.
[34] Tan, E.; Wilson, T. J.; Nahas, M. K.; Clegg, R. M.; Lilley, D. M. J.; Ha, T. A four-way junction accelerates hairpin ribozyme folding via a discrete intermediate. *Proc. Natl. Acad. Sci. USA* **2003**, *100*, 9308–9313.
[35] Diamond, J. M.; Turner, D. H.; Mathews, D. H. Thermodynamics of three-way multibranch loops in RNA. *Biochemistry* **2001**, *40*, 6971–6981.
[36] Benkato, K.; O'Brien, B.; Bui, M. N.; Jasinski, D. L.; Guo, P. X.; Khisamutdinov, E. F. Evaluation of thermal stability of RNA nanoparticles by temperature gradient gel electrophoresis (TGGE) in native condition. In *RNA Nanostructures*. Bindewald, E.; Shapiro, B. A., Eds.; Humana Press: New York, 2017; pp 123–133.
[37] Birkholz, O.; Burns, J. R.; Richter, C. P.; Psathaki, O. E.; Howorka, S.; Piehler, J. Multi-functional DNA nanostructures that puncture and remodel lipid membranes into hybrid materials. *Nat. Commun.* **2018**, *9*, 1521.
[38] Infante, R. E.; Radhakrishnan, A. Continuous transport of a small fraction of plasma membrane cholesterol to endoplasmic reticulum regulates total cellular cholesterol. *eLife* **2017**, *6*, e25466.
[39] Gerstle, Z.; Desai, R.; Veatch, S. L. Giant plasma membrane vesicles: An experimental tool for probing the effects of drugs and other conditions on membrane domain stability. *Methods Enzymol.* **2018**, *603*, 129–150.
[40] Sezgin, E.; Kaiser, H. J.; Baumgart, T.; Schwille, P.; Simons, K.; Levental, I. Elucidating membrane structure and protein behavior using giant plasma membrane vesicles. *Nat. Protoc.* **2012**, *7*, 1042–1051.
[41] Lin, C. M.; Li, C. S.; Sheng, Y. J.; Wu, D. T.; Tsao, H. K. Size-dependent properties of small unilamellar vesicles formed by model lipids. *Langmuir* **2012**, *28*, 689–700.
[42] Adler, J.; Parmryd, I. Quantifying colocalization by correlation: The pearson correlation coefficient is superior to the mander's overlap coefficient. *Cytometry A* **2010**, *77A*, 733–742.
[43] Dunn, K. W.; Kamocka, M. M.; McDonald, J. H. A practical guide to evaluating colocalization in biological microscopy. *Am. J. Physiol. Cell Physiol.* **2011**, *300*, C723–C742.
[44] Zhou, Y. M.; Dai, Z. F. New strategies in the design of nanomedicines to oppose uptake by the mononuclear phagocyte system and enhance cancer therapeutic efficacy. *Chem. Asian J.* **2018**, *13*, 3333–3340.
[45] Monopoli, M. P.; Åberg, C.; Salvati, A.; Dawson, K. A. Biomolecular coronas provide the biological identity of nanosized materials. *Nat. Nanotechnol.* **2012**, *7*, 779–786.
[46] Monopoli, M. P.; Walczyk, D.; Campbell, A.; Elia, G.; Lynch, I.; Bombelli, F. B.; Dawson, K. A. Physical-chemical aspects of protein corona: Relevance to *in vitro* and *in vivo* biological impacts of nanoparticles. *J. Am. Chem. Soc.* **2011**, *133*, 2525–2534.
[47] Saie, A. A.; Ray, M.; Mahmoudi, M.; Rotello, V. M. Engineering the nanoparticle-protein interface for cancer therapeutics. In *Nanotechnology-Based Precision Tools for the Detection and Treatment of Cancer*. Mirkin, C. A.; Meade, T. J.; Petrosko, S. H.; Stegh, A. H., Eds.; Springer: Cham, 2015; pp 245–273.
[48] Caracciolo, G.; Farokhzad, O. C.; Mahmoudi, M. Biological identity of nanoparticles *in vivo*: Clinical implications of the protein corona. *Trends Biotechnol.* **2017**, *35*, 257–264.
[49] Tsoi, K. M.; MacParland, S. A.; Ma, X. Z.; Spetzler, V. N.; Echeverri, J.; Ouyang, B.; Fadel, S. M.; Sykes, E. A.; Goldaracena, N.; Kaths, J. M. et al. Mechanism of hard-nanomaterial clearance by the liver. *Nat. Mater.* **2016**, *15*, 1212–1221.
[50] Zhang, Y. N.; Poon, W.; Tavares, A. J.; McGilvray, I. D.; Chan, W. C. W. Nanoparticle-liver interactions: Cellular uptake and hepatobiliary elimination. *J. Control. Release* **2016**, *240*, 332–348.
[51] Tenzer, S.; Docter, D.; Kuharev, J.; Musyanovych, A.; Fetz, V.; Hecht, R.; Schlenk, F.; Fischer, D.; Kiouptsi, K.; Reinhardt, C. et al. Rapid formation of plasma protein corona critically affects nanoparticle pathophysiology. *Nat. Nanotechnol.* **2013**, *8*, 772–781.
[52] Du, B. J.; Yu, M. X.; Zheng, J. Transport and interactions of nanoparticles in the kidneys. *Nat. Rev. Mater.* **2018**, *3*, 358–374.
[53] Du, B. J.; Jiang, X. Y.; Das, A.; Zhou, Q. H.; Yu, M. X.; Jin, R. C.; Zheng, J. Glomerular barrier behaves as an atomically precise bandpass filter in a sub-nanometre regime. *Nat. Nanotechnol.* **2017**, *12*, 1096–1102.
[54] Amoozgar, Z.; Yeo, Y. Recent advances in stealth coating of nanoparticle drug delivery systems. *Wiley Interdiscip. Rev. Nanomed. Nanobiotechnol.* **2012**, *4*, 219–233.
[55] Hoshyar, N.; Gray, S.; Han, H. B.; Bao, G. The effect of nanoparticle size on *in vivo* pharmacokinetics and cellular interaction. *Nanomedicine (Lond)* **2016**, *11*, 673–692.